



UNIVERSITY OF LEEDS

This is a repository copy of *Impact of igneous intrusion and associated ground deformation on the stratigraphic record*.

White Rose Research Online URL for this paper:

<https://eprints.whiterose.ac.uk/184110/>

Version: Accepted Version

Article:

Dobb, EM, Magee, C orcid.org/0000-0001-9836-2365, Jackson, CA-L et al. (2 more authors) (2022) Impact of igneous intrusion and associated ground deformation on the stratigraphic record. Geological Society Special Publication, 525. ISSN 0305-8719

<https://doi.org/10.1144/SP525-2021-115>

© 2022 The Author(s). Published by The Geological Society of London. All rights reserved. This is an author produced version of an article, published in Geological Society Special Publication. Uploaded in accordance with the publisher's self-archiving policy.

Reuse

Items deposited in White Rose Research Online are protected by copyright, with all rights reserved unless indicated otherwise. They may be downloaded and/or printed for private study, or other acts as permitted by national copyright laws. The publisher or other rights holders may allow further reproduction and re-use of the full text version. This is indicated by the licence information on the White Rose Research Online record for the item.

Takedown

If you consider content in White Rose Research Online to be in breach of UK law, please notify us by emailing eprints@whiterose.ac.uk including the URL of the record and the reason for the withdrawal request.



eprints@whiterose.ac.uk
<https://eprints.whiterose.ac.uk/>

26 intrusion and associated ground deformation can be unravelled. We focus on a forced fold
27 that likely formed in the Early Cretaceous to accommodate intrusion of magma, but which
28 was later amplified by burial-related differential compaction of the host sedimentary
29 sequence. We show how: (1) marine channels and clinoforms may be deflected by syn-
30 depositional intrusion-induced forced folds; and (2) differential compaction can locally
31 change clinoforms depth post-deposition, potentially leading to erroneous interpretation of
32 shoreline trajectories. Our results demonstrate seismic geomorphological analysis can help us
33 better understand how magma emplacement translates into ground deformation, and how this
34 shapes the landform of volcanic regions.

35

36 **Introduction**

37 The development of volcanic landforms modifies Earth surface processes (e.g., Karlstrom et
38 al. 2018). For example, in addition to the construction of volcanoes through the eruption of
39 lava, subsurface magma emplacement and accumulation can create dome-like relief by
40 uplifting the overlying rock and free surface, producing a forced fold (e.g., van Wyk de Vries
41 et al. 2014; Magee et al. 2017b; Sigmundsson et al. 2018). Most studies of ancient and active
42 forced folds use the relationship between fold and intrusion geometry to unravel the
43 kinematics and dynamics of magma emplacement (e.g., Pollard & Johnson 1973; Jackson &
44 Pollard 1990; Hansen & Cartwright 2006; Reeves et al. 2018); this is critical to volcano
45 monitoring and hazard mitigation, given we can invert intrusion-induced ground deformation
46 to locate and track intruding magma volumes (Galland & Scheibert 2013; Segall 2013). We
47 also recognise that the production of surface relief through intrusion-induced forced folding
48 can modify sediment dispersal, although few studies have explored this in detail (e.g.,
49 Smallwood & Maresh 2002; Egbeni et al. 2014; Magee et al. 2014; Magee et al. 2017a).
50 Deciphering precisely how changes in geomorphology relate to magma plumbing system

51 dynamics is also critical to volcanic hazard assessment (e.g., van Wyk de Vries et al. 2014;
52 Karlstrom et al. 2018). Seismic geomorphological analysis potentially provides a powerful
53 tool for exploring the interaction between palaeosurface deformation, sediment systems, and
54 magmatism, but we have to be aware that burial-related differential compaction may modify
55 and obscure the stratigraphic record of these processes (e.g., Magee et al. 2019).

56 Here, we use 3D seismic reflection and borehole data from the Exmouth Plateau,
57 offshore NW Australia (Fig. 1A), to examine the formation of a forced fold above a laccolith
58 and its influence on the stratigraphic record of the overlying Barrow Group. We use seismic-
59 stratigraphic relationships (e.g., onlap, erosional truncation) to determine a likely Early
60 Cretaceous (Berriasian) age for intrusion. We show that marine channels and clinofolds
61 forming part of the Early Cretaceous Barrow Group were locally deflected around and onlap
62 onto the forced fold; these observations build on previous studies demonstrating that
63 intrusion-induced forced folds can control sediment dispersal (e.g., Smallwood & Maresh
64 2002; Magee et al. 2014; Magee et al. 2017a). We also show that burial-related differential
65 compaction modified the stratigraphic record of the area post-intrusion, causing clinofold
66 inflection points to appear locally elevated across the forced fold. If not recognised, this
67 change in the elevation of clinofold inflection points, driven by differential compaction, may
68 be misinterpreted as evidence of relative sea-level change. Our results highlight seismic
69 geomorphology is an important tool for understanding interactions between intrusion-induced
70 ground deformation, landscape development, and sediment dispersal in volcanic regions
71 based on study of ancient examples.

72

73 **Geological Setting**

74 The Exmouth Plateau is part of the North Carnarvon Basin, offshore NW Australia. The
75 plateau covers ~300,000 km², occurs at a depth of 0.8–4 km below the sea surface, and

76 comprises <10 km thick crystalline basement overlain by an up to 18 km thick sequence of
77 sedimentary rock (Fig. 1) (Willcox & Exon 1976; Exon et al. 1992; Longley et al. 2002;
78 Stagg et al. 2004; Direen et al. 2008). The North Carnarvon Basin formed through multiple
79 phases of extension between the Late Carboniferous and Early Cretaceous, as Australia and
80 Greater India rifted apart (Exon et al. 1982; Longley et al. 2002; Stagg et al. 2004). Rifting in
81 the Late Triassic-to-Early Jurassic and Late Jurassic-to-Early Cretaceous was accommodated
82 by the formation of normal faults that: (i) offset the dominantly fluvio-deltaic, siliciclastic
83 pre-rift succession of the Triassic and Mungaroo Formation; and (ii) accommodated a thin
84 siliciclastic sequence of Late Triassic and Jurassic shallow marine sandstones and siltstones
85 (e.g., Brigadier Formation and Murat Siltstone) and the deep marine Dingo Claystone (Figs
86 1B and C) (Willcox & Exon 1976; Tindale et al. 1998; Stagg et al. 2004; Bilal et al. 2018).
87 During the final phases of rifting, regional uplift and development of the Base Cretaceous
88 unconformity preceded rapid subsidence and the deposition of the northwards prograding
89 Barrow Group (Figs 1B and C) (Reeve et al. 2016; Paumard et al. 2018). Clinofolds within
90 the Barrow Group are ~100–550 m high and have slopes of 1–9°, indicating they define a
91 long, linear, ramp-like shelf-margin, rather than a discrete delta (e.g., Fig. 1C) (Paumard et al.
92 2018). The top of the Barrow Group is marked by a regional unconformity, which is capped
93 by the Zeepaard Formation and Birdrong Sandstone (Fig. 1B) (Reeve et al. 2016). Rifting
94 ceased in the Early Cretaceous, associated with the breakup of Australia and Greater India,
95 leading to thermal subsidence and development of a post-rift passive margin (Fig. 1B) (Stagg
96 et al. 2004; Gibbons et al. 2012). This transition to a passive margin was marked by the onset
97 of deposition of the deep marine Muderong Shale, within which a polygonal fault tier
98 subsequently formed (Fig. 1B) (Tindale et al. 1998).

99 Magmatism in the North Carnarvon Basin occurred periodically throughout the
100 Middle Jurassic-to-Early Cretaceous (Fig. 1B). A seismically high-velocity (~6.2–7.4 km s⁻¹)

101 body within the lower crust of the Exmouth Plateau is interpreted as a large magmatic body,
102 likely of mafic-to-ultramafic composition, emplaced during the Callovian (~165 Ma; Fig. 1B)
103 (Frey et al. 1998; Rey et al. 2008; Rohrman 2013, 2015). Spatially if perhaps not genetically
104 associated with this high-velocity body are: (i) a radial dyke swarm (the Exmouth Dyke
105 Swarm), which was emplaced at ~148 Ma (Tithonian; Fig. 1B) (Magee & Jackson 2020); and
106 (ii) a series of sills and sill-complexes, which seismic-stratigraphic dating of intrusion-
107 induced forced folds suggests were emplaced in the Kimmeridgian and Berriasian-to-
108 Valanginian (Figs 1B and C) (Symonds et al. 1998; Magee et al. 2013a, b; Magee et al.
109 2017a; Mark et al. 2020; Norcliffe et al. 2021). The final phase of igneous activity coincided
110 with continental break-up and the development of a continent-ocean transition zone outboard
111 of the Exmouth Plateau (Figs 1A and B) (Hopper et al. 1992; Direen et al. 2008; Reeve et al.
112 2021).

113

114 **Dataset and Methods**

115 *Data*

116 We use the Glencoe dataset, which is a zero-phase, time-migrated, 3D seismic reflection
117 survey (Figs 1A and 2). The survey covers an area of ~4042 km², has a line spacing of 25 m,
118 recorded to a depth of ~8 s two-way time (TWT), and is displayed with SEG (Society for
119 Exploration Geophysicists) positive polarity; i.e. a downward increase in acoustic impedance
120 correlates with a peak (red-yellow reflection), and a downward decrease in acoustic
121 impedance correlates with a trough (blue reflection). We map the upper and lower contacts of
122 the studied intrusion, as well as one horizon beneath it (the Top Mungaroo Formation), and
123 six horizons above; data from the nearby Chester-1ST1 and Chester-2 boreholes allow us to
124 identify the lithology and age of the sedimentary sequences containing these horizons (Fig.
125 2). To tie the wells and the seismic reflection data we create a synthetic seismogram using

126 Chester-1ST1 well-log (density and sonic velocity) and checkshot information from a depth
127 range of ~2.3–4.5 km TVD (true vertical depth) (Fig. 2C).

128 No boreholes intersect the intrusion or fold studied here, so we cannot directly
129 constrain their composition or physical properties (e.g., seismic velocity) (Fig. 2A). Due to
130 this lack of borehole data, and because the possible seismic velocity range (4.0–7.5 km s⁻¹) of
131 igneous intrusions is rather large (see Magee et al. 2015 and references therein), we do not
132 depth-convert the seismic reflection data. Instead, we depth-convert measurements in seconds
133 TWT for the intrusion and folded sedimentary sequence using: (i) seismic velocities of ~5.55
134 (±10%) km s⁻¹ for the intrusion, which marks the typical range of mafic igneous rocks
135 (Skogly 1998; Planke et al. 2005) similar to the basaltic sill and dyke penetrated in the nearby
136 Rimfire-1 and Chester-1ST1 boreholes (Fig. 2A) (Moig & Massie 2010; Childs et al. 2013);
137 and (ii) the time-depth relationship for the sedimentary sequence determined from the
138 checkshot data for nearby boreholes (i.e. Briseis-1, Chester-1ST1, Glencoe-1, Nimblefoot-1,
139 and Warrior-1; Fig. 2A), which indicates the Barrow Group and the underlying folded
140 sequence has an interval velocity of ~3.0 (±0.5) km s⁻¹ (Supplementary Figure 1;
141 Supplementary Table 1). These seismic velocity ranges, coupled with measurements of
142 dominant frequency, also allow us to estimate the data resolution. We define the limit of
143 separability ($\lambda/4$, where λ is the dominant wavelength), i.e. the minimum vertical distance
144 between two boundaries required to produce two distinct reflections, and the limit of
145 visibility ($\lambda/30$) below which reflections cannot be distinguished from noise (Brown 2011). If
146 the vertical distance between boundaries is less than the limit of separability, but greater than
147 the limit of visibility, the reflections from these boundaries will merge on their return to the
148 surface and cannot be deconvolved, producing a tuned reflection package rather than two
149 distinct reflections (Widess 1973; Brown 2011). The dominant frequency of the data in the
150 study area is ~25 Hz, indicating the limit of separability is ~56 (±6) m and the limit of

151 visibility is $\sim 7 (\pm 1)$ m for the intrusion (Norcliffe et al. 2021). For the Barrow Group and
152 folded sequence, the limits of separability and visibility are $\sim 30 (\pm 5)$ m and $\sim 4 (\pm 1)$ m,
153 respectively. The horizontal resolution of the time-migrated seismic reflection data is likely
154 up to $\sim 30 (\pm 5)$ m (i.e. $\lambda/4$).

155

156 **Results**

157 *Intrusion seismic expression, geometry, and stratigraphic context*

158 The intrusion is elliptical, elongated NE, ~ 4.5 km long, and can be sub-divided into two
159 components: (i) a tabular, strata-concordant main body (3.9×2.5 km) that on average is ~ 104
160 ms TWT thick ($\sim 260\text{--}317$ m assuming a velocity of $\sim 5.55 (\pm 10\%)$ km s⁻¹), but which is
161 locally up to ~ 202 ms TWT thick ($\sim 504\text{--}617$ m); and (ii) encompassing inclined sheets,
162 expressed as tuned reflection packages, which transgress upwards from (up to ~ 180 ms TWT
163 or $\sim 225\text{--}315$ m high) and dip in towards the main body (Figs 2B, C, and 3). The intrusion
164 occurs within a NE-trending graben and is encased by Late Triassic-to-Jurassic strata (Figs
165 2B and C). Both the top and base contacts of the intrusion main body are resolved, with the
166 Top Intrusion contact corresponding to a high amplitude, continuous, positive polarity
167 reflection (Figs 2B and C). The Base Intrusion contact corresponds to a moderate-to-high
168 amplitude, negative polarity reflection that broadly coincides with the Top Mungaroo
169 Formation (Figs 2B and C). There is an up to ~ 57 ms TWT ($\sim 71\text{--}100$ m) high, NE-trending
170 ridge along the centre of the main intrusion (Fig. 3C), with the Top Intrusion contact lower on
171 its western side (Fig. 3A); the ridge is not seen on the Base Intrusion contact (Fig. 3B).

172

173 *Stratigraphic and structural framework*

174 The Top Mungaroo Formation is expressed as a high amplitude, negative polarity reflection
175 that is offset by planar and arcuate, \sim NE-SW striking normal faults (purple horizon in Fig. 2);

176 this overall structural framework is mirrored by a prominent unconformity at shallower
177 depths (Fig. 4A), which is expressed as a moderate-to-high amplitude, positive polarity
178 reflection (Figs 2B and C). At Chester-1ST1, this unconformity is underlain by the
179 Pliensbachian Murat Siltstone and overlain by downthrown Berrisian Barrow Group rocks
180 (Fig. 2). However, at Chester-2, closer to the study area, the prominent unconformity is
181 overlain by a thin (<10 m thick) package of Tithonian Dingo Claystone, implying it likely
182 corresponds to the Callovian unconformity (Fig. 2). Unlike the Top Mungaroo Formation, the
183 Callovian unconformity is locally uplifted by up to ~200 ms TWT (~250–350 m) directly
184 above the intrusion, relative to its regional trend (blue horizon in Figs 2B and C, Fig. 4A).
185 This uplift of the Callovian unconformity occurs at an abrupt offset, i.e. an annular vertical
186 fault, coincident with the lateral edge of the intrusion (Figs 2B and C, Fig. 4A). Within the
187 uplifted section of the Callovian unconformity, a narrow graben bound by NE-SW striking
188 normal faults with throws of $\lesssim 60$ ms TWT ($\lesssim 75$ – 105 m) is present, along with several minor
189 intra-graben faults (Figs 2B, C, and 4A). These NE-SW striking faults extend down to the
190 ridge expressed along the Top Intrusion contact, and are broadly parallel to but are physically
191 separate from, those outside the area of uplift (Figs 2B, C, and 4A).

192 Above the Callovian unconformity, Horizon 1 also displays an area of uplift above the
193 intrusion but there is less evidence of faulting across its extent, although its lack of lateral
194 continuity means it can only be locally mapped (green dashed horizon in Figs 2B, C, and 4B).
195 Horizon 1 appears to onlap onto an underlying reflection before reaching the Chester-1ST1
196 borehole, such that we cannot determine its absolute age (Fig. 2C). However, the reflection
197 Horizon 1 onlaps onto occurs ~40 ms TWT (~50–70 m) above the Callovian unconformity,
198 suggesting it is Berrisian in age (Fig. 2C). In contrast to the abrupt uplift of the Callovian
199 unconformity across a sub-vertical, annular fault, Horizon 1 uplift is marked by a gradual
200 folding of strata (Figs 2B and C). The fold is a $\sim 4.8 \times 3.3$ km, flat-topped dome with a

201 monoclinial rim and covers a greater area than the underlying intrusion (Fig. 4B). The current
202 maximum amplitude of the fold is ~120 ms TWT (~150–210 m) (Fig. 4B). In places,
203 immediately overlying reflections onlap the folded Horizon 1 (Fig. 2B). The Horizon 1
204 reflection displays a positive polarity and has an overall moderate amplitude, although there
205 is a NNW-trending, 1–2 km wide zone where the reflection has a high amplitude (Figs 2B, C,
206 and 4B). This high amplitude zone appears to deviate around the fold (Fig. 3B). Between the
207 Callovian unconformity and Horizon 1 there is a clear thickening of the stratal package (up to
208 ~225 ms TWT, or ~281–393 m, thick) within the graben hosting the intrusion (Figs 2B, C,
209 and 4C). A zone of marked thinning interrupts this thickening trend and coincides with the
210 area of uplift above the intrusion; here the Callovian unconformity to Horizon 1 strata is
211 $\lesssim 137$ ms TWT ($\lesssim 171$ –239 m) thick (Fig. 4C). The NE-SW striking graben within the area of
212 uplift hosts a thicker (~34–40 ms TWT, or 42–70 m, thick) succession of the Callovian
213 unconformity to Horizon 1 strata compared to its flanks (Fig. 4C).

214 Horizon 2 corresponds to a moderate amplitude, positive polarity reflection that, like
215 Horizon 1, displays little evidence of faulting and a prominent flat-topped fold (green horizon
216 with black outline in Figs 2B and C, Fig. 4D). The fold at Horizon 2 is $\sim 5.0 \times 3.5$ km, larger
217 than the fold area expressed at Horizon 1 and that of the intrusion, and its current maximum
218 amplitude is ~150 ms TWT (~191–268 m) (Fig. 4D). Between Horizon 1 and Horizon 2 there
219 is a gradual westward thickening of strata regionally (Figs 2B, C, and 4E). Across the fold,
220 the strata bound by Horizon 1 and Horizon 2 locally thins to $\lesssim 50$ ms TWT ($\lesssim 63$ –88 m),
221 except where it thickens to ~100 ms TWT (~125–175 m) into the intra-fold graben expressed
222 along the Callovian unconformity (Figs 2B, C, and 4E). Reflections immediately above
223 Horizon 2 dip gently to the NE and correspond to the toesets of Barrow Group clinoforms
224 (Figs 2B, C, and 4F). These clinoform reflections, including Horizon 3, onlap onto the fold
225 and are absent across the north-western part of the fold (Figs 2B, C, and 4F). Above Horizon

226 3, younger clinoforms reflections that dip to the NE and cover the fold locally have inflection
227 points that occur at structurally shallower levels than those beyond the fold limit (Figs 2B and
228 C). The supra-intrusion fold is also expressed at the Top Barrow Group (green solid horizon),
229 where it has a maximum amplitude of ~50 ms TWT (~63–88 m), up to the Top Muderong
230 Shale (light green horizon), where its maximum amplitude is ~40 ms TWT (~50–70 m) (Figs
231 2B, C, 4G and H). A key observation is that with the exception of the Top Barrow Group, no
232 reflections onlap onto the fold above Horizon 2 (Figs 2B and C); at the Top Barrow,
233 overlying reflections do onlap onto the horizon but do so regionally, not just across the fold
234 (Figs 2B and C). Strata between both Horizon 2 and Top Barrow Group, as well as the Top
235 Barrow Group to Top Muderong Shale, display subtle thinning across the fold, but around its
236 immediate periphery there is a zone of local thickening (Figs 4I and J).

237

238 **Discussion**

239 The mapped intrusion is dominated by a tabular main body that is consistently ~261–319 m
240 thick, except where a NE-trending ridge is developed along the top contact. The main body is
241 encompassed by centrally dipping inclined sheets (Figs 2B, C, and 3). The intrusion is only
242 ~4.5 km long (Fig. 3A) and thus has a length-to-thickness ratio of ~15, which suggests it can
243 be defined as either a laccolith or sill (Cruden et al. 2017); given its greater thickness
244 compared to previously identified sills offshore NW Australia (e.g., Magee et al., 2013a, b;
245 Mark et al., 2020), we favour describing the intrusion as a laccolith. Given the spatial
246 restriction of the dome-shaped fold above the laccolith, we consider it a forced fold that
247 formed either (Fig. 5): (i) to make space for the intruding magma volume (Pollard & Johnson
248 1973; Hansen & Cartwright 2006; Jackson et al. 2013); and/or (ii) via later differential
249 compaction as the porosity of the sedimentary strata adjacent to the laccolith gradually
250 reduces during burial, whilst the thickness of the incompressible intrusion remains constant

251 (Schmiedel et al. 2017; Magee et al. 2019). To determine the possible impact of intrusion-
252 related deformation on surface morphology and sediment dispersal, we first need to establish
253 how and when the forced fold developed (Smallwood & Maresh 2002; Magee et al. 2017a).

254

255 *Folding mechanisms and timing*

256 Deformation related to the laccolith appears to affect strata situated just above the Top
257 Mungaroo Formation up to the Top Muderong Shale (Figs 2 and 4). In the lowermost section
258 of this sedimentary sequence, below the Callovian unconformity, deformation is related to
259 sub-vertical faults located along the laccolith edge (Figs 2B, C, and 3A). Similar relationships
260 between tabular intrusions, faults, and overburden uplift are recognised in a variety of
261 geological settings, as well as physical and numerical models, where deformation is driven by
262 magma emplacement (de Saint-Blanquat et al. 2006; Magee et al. 2017a; Montanari et al.
263 2017). In contrast to strata below the Callovian unconformity, which are largely faulted,
264 strata above this unconformity are primarily deformed by folding (Figs 2 and 4). At both
265 Horizon 1 and Horizon 2, we observe overlying reflections onlapping onto the fold (Figs 2B,
266 C, 4E, and F), which indicates the surface was locally uplifted and deposition was restricted
267 across its crest; i.e. horizons 1 and 2 mark palaeosurfaces that were contemporaneous to a
268 phase of fold development (Trude et al. 2003). We also note that within the folded strata,
269 between Horizon 1 and the laccolith top, two graben-bounding normal faults and associated
270 minor normal faults are developed (Figs 2B, C, and 4A). Although these normal faults within
271 the fold are typically NE-trending and parallel to many of the large tectonic normal faults in
272 the area, they do not extend beyond the fold limits (Fig. 4A). Similar normal faults have been
273 observed in natural and modelled intrusion-induced forced folds, and occur in response to
274 outer-arc extension generated during the bending of strata above intruding magma (Pollard &
275 Johnson 1973; Magee et al. 2013b; Montanari et al. 2017). Based on the structure and

276 seismic-stratigraphic relationships of the forced fold below Horizon 2, and their similarity to
277 intrusion-induced forced folds elsewhere, we suggest space for magma emplacement was, at
278 least partly, generated by overburden uplift (Figs 5A, 6A, and B). Although it is difficult to
279 establish the age of Horizon 1, we know it was deposited after formation of the Callovian
280 unconformity and before progradation of the Barrow Group clinoforms into the study area in
281 the Berriasian (Fig. 2C). Seismic-stratigraphic relationships further suggest Horizon 1 onlaps
282 onto a reflection located >50 m above the Callovian unconformity at Chester-2, and thus >40
283 m above the Tithonian strata preserved here (Fig. 2C). We suggest magma emplacement and
284 folding likely began in the Berriasian, when Horizon 1 represented the surface, and involved
285 erosion of strata above the Callovian unconformity across its crest (Fig. 6A) (Trude et al.
286 2003); we consider that this erosion produced the observed thinning of the Callovian
287 unconformity to Horizon 1 strata across the forced fold (Fig. 4C). With laccolith inflation and
288 continued folding, bending-related stresses likely instigated faulting around the intrusion
289 periphery and fold crest, facilitating uplift and perhaps providing pathways for magma ascent
290 and inclined sheet formation (Fig. 6B) (Pollard & Johnson 1973; Jackson & Pollard 1990;
291 Thomson & Schofield 2008). However, we lack the data resolution to determine whether
292 intrusion and folding (and faulting) occurred continuously up to when the Horizon 2 marked
293 the surface, or if their growth were incremental (Trude et al. 2003; Magee et al., 2017a;
294 Reeves et al. 2018).

295 Above Horizon 2, the forced fold is subtly expressed at several horizons up to the Top
296 Muderong Shale (Figs 2B, C, and 4). Throughout the Horizon 2 to Top Muderong Shale
297 succession, we only observe onlap onto the fold at the Top Barrow Group, but note this
298 horizon is equivalent to a regional unconformity and onlap of overlying reflections also
299 occurs regionally beyond the fold limits (Figs 2B and C). On thickness maps of Horizon 2 to
300 the Top Barrow Group, as well as the Top Barrow Group to Top Muderong Shale, it is

301 apparent that the strata thins across the fold and there is a zone of increased thickness
302 encircling but beyond the fold periphery (Figs 4I and J). These thickening patterns and the
303 lack of onlapping reflections local onto the forced fold are consistent with its formation via
304 post-emplacement, differential compaction during burial (Figs 5B and 6C) (Hansen &
305 Cartwright 2006; Jackson et al. 2013; Schmiedel et al. 2017).

306

307 *Influence of intrusion-related ground deformation on the stratigraphic record*

308 Having established that laccolith emplacement induced surface uplift likely in the Early
309 Cretaceous, we now examine its effect on sedimentation patterns. First, the occurrence of
310 onlapping reflections onto the forced fold at horizons 1 and 2 demonstrates intrusion-induced
311 uplift can locally restrict deposition (Figs 2B, C, and 4F). For example, the mapped
312 distribution of Horizon 3 indicates the north-eastwards progradation of Barrow Group
313 clinoforms were locally impeded by relief associated with the forced fold (Fig. 4F) (Reeve et
314 al. 2016; Paumard et al. 2018). There is also a possible channel feature developed along
315 Horizon 1, expressed as a NNW-trending, <2 km wide high amplitude zone, which appears to
316 deviate around the forced fold (Figs 2B, C, and 4B); i.e. the possible channel thins
317 northwards and locally trends NW (as opposed to NNW) where it encounters the southern
318 edge of the forced fold (Fig. 4B). We suggest that as this channel progressed northwards and
319 encountered the seabed relief created by the forced fold, it followed the contours and flowed
320 around the folds western side (Fig. 4B), similar to observations of other fold-channel
321 interactions (e.g., Smallwood & Maresh, 2002; Magee et al. 2014). Overall, our results,
322 coupled with observations of surface uplift at active volcanoes, demonstrate that ground
323 deformation driven by magma emplacement can instigate abrupt changes in geomorphology
324 and sediment dispersal, which may be modified over years to millions of years as intrusion

325 (periodically) continues (Smallwood & Maresh 2002; Egbeni et al. 2014; Magee et al. 2014;
326 Magee et al. 2017a; Reeves et al. 2018).

327 A key aspect of studying palaeosurface geomorphology with seismic reflection data is
328 determining whether mapped horizons have been modified post-burial. Our work supports
329 previous studies that show differential compaction of strata across an area hosting a solidified
330 igneous intrusion can produce a forced fold, independent of magma emplacement (Hansen &
331 Cartwright 2006; Jackson et al. 2013; Schmiedel et al. 2017). Importantly, we observe
332 inflection points of the Barrow Group clinoforms to be situated at shallower structural levels
333 within the forced fold compared to beyond its limit (Figs 2B and C). If such differential
334 compaction was not recognised or explicitly accounted for, variations in clinoform trajectory
335 might erroneously be interpreted as evidence for changes in relative sea level; i.e., apparent
336 rising trajectories on the landward side of the forced fold record sea-level rise, whereas
337 falling trajectories on the seaward side record sea-level fall (e.g., Steel et al. 2002). Yet if we
338 account for differential compaction by flattening the Top Barrow Group, we see that there is
339 no local change in clinoform inflection trajectory (Fig. 7). Considering how differential
340 compaction may affect subsurface structures in volcanic areas, where incompressible
341 intrusive or extrusive igneous rocks occur, is critical to properly assessing palaeosurface
342 geomorphology (Clairmont et al. 2021).

343

344 **Conclusions**

345 Unravelling how magma emplacement translates into ground deformation can help us
346 evaluate potential volcanic hazards in areas where we cannot directly access the subsurface.
347 As part of our endeavour to improve hazard assessment, we need to better understand how
348 volcanic landforms evolve through time and interact with surface processes. Seismic
349 reflection geomorphology offers an exciting opportunity to study active and ancient volcanic

350 landforms in 3D. Here we use 3D seismic reflection data from offshore NW Australia to
351 study a laccolith and overlying forced fold. By identifying seismic-stratigraphic onlap onto
352 the forced fold we demonstrate magma emplacement instigated overburden uplift in the Early
353 Cretaceous. Associated ground deformation restricted sediment deposition and deflected a
354 channel within the overlying Barrow Group, a package of deep-water shelf margin
355 clinoforms. With continued deposition and burial of the study area, differential compaction
356 produced a forced fold on top of that generated by magma emplacement; i.e. strata adjacent
357 to the laccolith were able to compact but the intrusion itself was relatively incompressible,
358 limiting subsidence of the overlying sedimentary column. We demonstrate that differential
359 compaction locally modified the relative position of clinoform inflection points, which if not
360 recognised can be misinterpreted as a systems tract variation. Overall, our study serves to
361 highlight the possible benefits and complications of seismic geomorphology in volcanic
362 areas.

363

364 **Acknowledgements**

365 This study formed represents work conducted by ED during their MSci undergraduate
366 project. The seismic and well data are open access and can be found through Geoscience
367 Australia (www.ga.gov.au/nopims) to whom we are grateful. We also acknowledge
368 Schlumberger for providing Petrel seismic interpretation software. We thank two reviewers
369 for their constructive comments, and Elodie Lebas for editorial handling.

370

371 **Figure captions**

372 Figure 1: (A) Offshore NW Australia map showing key tectonic and basin elements
373 (modified from Norcliffe et al. 2021). NCB = North Carnarvon Basin, SCB = South
374 Carnarvon Basin, ExSB = Exmouth Sub-basin, BSB = Barrow Sub-basin, DSB = Dampier

375 Sub-basin, PS = Peedamullah Shelf, WP = Wallaby Plateau, CAP = Cuvier Abyssal Plain,
376 GAP = Gascoyne Abyssal Plain, AAP = Argo Abyssal Plain, CRFZ Cape Range Fracture
377 Zone. Elevation data from the 2009 Australian Bathymetry and Topography grid (Geoscience
378 Australia). (B) Stratigraphic column for the Exmouth Plateau highlighting important tectonic
379 and magmatic events (based on Hocking et al. 1987; Hocking 1992; Tindale et al. 1998;
380 Longley et al. 2002; Magee & Jackson 2020). (C) Uninterpreted and interpreted 2D seismic
381 line across the Exmouth Plateau and Exmouth Sub-basin (taken from Norcliffe et al. 2021).
382 See (A) for location.

383

384 Figure 2: (A) Time-structure map of the Top Mungaroo Formation across the Glencoe 3D
385 survey. See location in Fig. 1A. Boreholes shown are 1 = Chester-1ST1; 2 = Warrior-1; 3 =
386 Nimblefoot-1; 4 = Rimfire-1; 5 = Glencoe-1; 6 = Briseis-1; 7 = Chester-2. (B and C)
387 Uninterpreted and interpreted seismic sections showing the structural and stratigraphic
388 framework of the studied intrusion and fold. In (C) we show the synthetic well-tie between
389 the seismic section and Chester-1ST1, which we created by using well-log (density = RHOB
390 (blue); sonic velocity = DT (black)) and checkshot data to produce a sonic calibration and
391 time-depth relationship. A Ricker wavelet of 25 Hz was used to create the synthetic
392 seismogram. TVD is true vertical depth (km) and TWT is two-way time (seconds). See (A)
393 for locations.

394

395 Figure 3: Time-structure maps of the Top (A) and Base (B) Intrusion reflections, and (C) the
396 vertical thickness map of the intrusion where both the top and base reflections have been
397 distinguished in the data. The yellow dashed line outlines the main body of the intrusion. Dark
398 gray corresponds to areas beyond the intrusion limits.

399

400 Figure 4: Time-structure and thickness maps (in ms TWT) for the interpreted horizons. For
401 Horizon 1 (B), we also show an RMS (root-mean square) amplitude map to highlight the
402 presence of a possible channel.

403

404 Figure 5: Schematics showing the two end-member processes for forming forced folds above
405 intrusions: (A) syn-emplacement uplift to generate space for the intruding magma; and (B)
406 post-emplacement differential compaction that occurs during burial of the sedimentary
407 sequence (modified from Magee et al. 2014).

408

409 Figure 6: Schematics showing our interpretation of laccolith emplacement and forced folding.
410 (A) Intrusion emplacement and inflation in the first stage are spatially accommodated by
411 overburden uplift, but erosion of the contemporaneous surface (i.e. Horizon 1) across the fold
412 removes material. (B) In the second stage, after deposition of sediment onlapping onto the
413 fold at Horizon 1, continued or renewed magma emplacement and laccolith inflation drive
414 further uplift. (C) The final phase of fold development occurs after magma emplacement
415 ceases, whereby the sedimentary column adjacent to the laccolith compacts more than that
416 above the intrusion (i.e. differential compaction).

417

418 Figure 7: Uninterpreted (A) and interpreted (B) seismic section shown in Figure 2B, but here
419 we have flattened the data on the Top Barrow Group horizon to show the likely original
420 clinoforms geometry. See Figure 2A for line location.

421

422 **References**

423 Bilal, A., McClay, K. & Scarselli, N. 2018. Fault-scarp degradation in the central Exmouth
424 Plateau, North West Shelf, Australia. *Geological Society, London, Special Publications*, **476**,
425 SP476. 411.

426

427 Brown, A.R. 2011. *Interpretation of three-dimensional seismic data*. 6th ed. AAPG and SEG,
428 Oklahoma, USA, 665 p.
429

430 Childs, K., Banfield, J., Jakymec, M. & Jones, A. 2013. *Well Completion Report: Chester-1*
431 *& Chester-1 ST1 interpretative data*. Hess, 353 p.
432

433 Clairmont, R., Kolawole, F., Omale, A.P. & Bedle, H. 2021. Controls of pre-existing
434 structures on clinoform architecture and the associated progradational system elements. *Basin*
435 *Research*, **33**, 875-902.
436

437 Cruden, A., McCaffrey, K. & Bungler, A. 2017. Geometric scaling of tabular igneous
438 intrusions: Implications for emplacement and growth. In: Breitkreuz C., Rocchi S. (eds)
439 *Physical Geology of Shallow Magmatic Systems*, Advances in Volcanology, Springer, Cham,
440 11-38.
441

442 de Saint-Blanquat, M., Habert, G., Horsman, E., Morgan, S.S., Tikoff, B., Launeau, P. &
443 Gleizes, G. 2006. Mechanisms and duration of non-tectonically assisted magma emplacement
444 in the upper crust: the Black Mesa pluton, Henry Mountains, Utah. *Tectonophysics*, **428**, 1-
445 31.
446

447 Direen, N.G., Stagg, H.M.J., Symonds, P.A. & Colwell, J.B. 2008. Architecture of volcanic
448 rifted margins: new insights from the Exmouth – Gascoyne margin, Western Australia.
449 *Australian Journal of Earth Sciences*, **55**, 341-363.
450

451 Egbeni, S., McClay, K., Jian-kui Fu, J. & Bruce, D. 2014. Influence of igneous sills on
452 Paleocene turbidite deposition in the Faroe–Shetland Basin: a case study in Flett and Muckle
453 sub-basin and its implication for hydrocarbon exploration. *Geological Society, London,*
454 *Special Publications*, **397**, 33-57.
455

456 Exon, N., Von Rad, U. & Von Stackelberg, U. 1982. The geological development of the
457 passive margins of the Exmouth Plateau off northwest Australia. *Marine Geology*, **47**, 131-
458 152.
459

460 Exon, N., Haq, B. & Von Rad, U. 1992. Exmouth Plateau revisited: scientific drilling and
461 geological framework. *Proceedings of the Ocean Drilling Program, Scientific Results*, 3-20.
462

463 Frey, Ø., Planke, S., Symonds, P.A. & Heeremans, M. 1998. Deep crustal structure and
464 rheology of the Gascoyne volcanic margin, western Australia. *Marine Geophysical*
465 *Researches*, **20**, 293-311.
466

467 Galland, O. & Scheibert, J. 2013. Analytical model of surface uplift above axisymmetric flat-
468 lying magma intrusions: Implications for sill emplacement and geodesy. *Journal of*
469 *Volcanology and Geothermal Research*, **253**, 114-130.
470

471 Gibbons, A.D., Barckhausen, U., den Bogaard, P., Hoernle, K., Werner, R., Whittaker, J.M.
472 & Müller, R.D. 2012. Constraining the Jurassic extent of Greater India: Tectonic evolution of
473 the West Australian margin. *Geochemistry, Geophysics, Geosystems*, **13**, Q05W13.
474

475 Hansen, D.M. & Cartwright, J. 2006. The three-dimensional geometry and growth of forced
476 folds above saucer-shaped igneous sills. *Journal of Structural Geology*, **28**, 1520-1535.

477
478 Hocking, R. 1992. Jurassic deposition in the southern and central North West Shelf. *Western*
479 *Australia: Geological Survey Western Australia Record*, Record **1992/7**, 108 p.
480
481 Hocking, R.M., Moors, H.T. & Van de Graaff, W.E. 1987. *Geology of the carnarvon basin,*
482 *Western Australia.* State Print. Division.
483
484 Hopper, J.R., Mutter, J.C., Larson, R.L. & Mutter, C.Z. 1992. Magmatism and rift margin
485 evolution: Evidence from northwest Australia. *Geology*, **20**, 853-857.
486
487 Jackson, C.A.-L., Schofield, N. & Golenkov, B. 2013. Geometry and controls on the
488 development of igneous sill-related forced folds: A 2-D seismic reflection case study from
489 offshore southern Australia. *Geological Society of America Bulletin*, **125**, 1874-1890.
490
491 Jackson, M.D. & Pollard, D.D. 1990. Flexure and faulting of sedimentary host rocks during
492 growth of igneous domes, Henry Mountains, Utah. *Journal of Structural Geology*, **12**, 185-
493 206.
494
495 Karlstrom, L., Richardson, P.W., O'Hara, D. & Ebmeier, S.K. 2018. Magmatic landscape
496 construction. *Journal of Geophysical Research: Earth Surface*, **123**, 1710-1730.
497
498 Longley, I., Buessenschuett, C., Clydsdale, L., Cubitt, C., Davis, R., Johnson, M., Marshall,
499 N., Murray, A., *et al.* 2002. The North West Shelf of Australia—a Woodside perspective. *The*
500 *sedimentary basins of Western Australia*, **3**, 27-88.
501
502 Magee, C. & Jackson, C.-L. 2020. Seismic reflection data reveal the 3D structure of the
503 newly discovered Exmouth Dyke Swarm, offshore NW Australia. *Solid Earth*, **11**, 576-606.
504
505 Magee, C., Jackson, C.A.-L. & Schofield, N. 2013a. The influence of normal fault geometry
506 on igneous sill emplacement and morphology. *Geology*, **41**, 407-410.
507
508 Magee, C., Briggs, F. & Jackson, C.A.-L. 2013b. Lithological controls on igneous intrusion-
509 induced ground deformation. *Journal of the Geological Society*, **170**, 853-856.
510
511 Magee, C., Jackson, C.L. & Schofield, N. 2014. Diachronous sub-volcanic intrusion along
512 deep-water margins: insights from the Irish Rockall Basin. *Basin Research*, **26**, 85-105.
513
514 Magee, C., Maharaj, S.M., Wrona, T. & Jackson, C.A.-L. 2015. Controls on the expression of
515 igneous intrusions in seismic reflection data. *Geosphere*, **11**, 1024-1041.
516
517 Magee, C., Jackson, C.A.-L., Hardman, J.P. & Reeve, M.T. 2017a. Decoding sill
518 emplacement and forced fold growth in the Exmouth Sub-basin, offshore northwest
519 Australia: Implications for hydrocarbon exploration. *Interpretation*, **5**, SK11-SK22.
520
521 Magee, C., Bastow, I.D., de Vries, B.v.W., Jackson, C.A.-L., Hetherington, R., Hagos, M. &
522 Hoggett, M. 2017b. Structure and dynamics of surface uplift induced by incremental sill
523 emplacement. *Geology*, **45**, 431-434.
524

525 Magee, C., Hoggett, M., Jackson, C.A.-L. & Jones, S.M. 2019. Burial-Related Compaction
526 Modifies Intrusion-Induced Forced Folds: Implications for Reconciling Roof Uplift
527 Mechanisms Using Seismic Reflection Data. *Frontiers in Earth Science*, **7**, 37.
528

529 Mark, N., Holford, S.P., Schofield, N., Eide, C.H., Pugliese, S., Watson, D. & Muirhead, D.
530 2020. Structural and lithological controls on the architecture of igneous intrusions: examples
531 from the NW Australian Shelf. *Petroleum Geoscience*, **26**, 50-69.
532

533 Moig, N & Massie, S. 2010. *Well Completion Report, Rimfire-1, Interpretative data*. Hess
534 Exploration Australia Pty Limited, 62 p.
535

536 Montanari, D., Bonini, M., Corti, G., Agostini, A., Del Ventisette, C.J.J.o.V. & Research, G.
537 2017. Forced folding above shallow magma intrusions: Insights on supercritical fluid flow
538 from analogue modelling. **345**, 67-80.
539

540 Norcliffe, J., Magee, C., Jackson, C., Kopping, J. & Lathrop, B. 2021. Fault inversion
541 contributes to ground deformation above inflating igneous sills. *Volcanica*, **4**, 1-21.
542

543 Paumard, V., Bourget, J., Payenberg, T., Ainsworth, R.B., George, A.D., Lang, S.,
544 Posamentier, H.W. & Peyrot, D. 2018. Controls on shelf-margin architecture and sediment
545 partitioning during a syn-rift to post-rift transition: Insights from the Barrow Group (Northern
546 Carnarvon Basin, North West Shelf, Australia). *Earth-Science Reviews*, **177**, 643-677.
547

548 Planke, S., Rasmussen, T., Rey, S.S. & Myklebust, R. 2005. Seismic characteristics and
549 distribution of volcanic intrusions and hydrothermal vent complexes in the Vøring and Møre
550 basins. In: Doré, A.G. (ed) *Petroleum Geology: North-West Europe and Global Perspectives*
551 *- Proceedings of the 6th Petroleum Geology Conference*. Geological Society, London, 833-
552 844.
553

554 Pollard, D.D. & Johnson, A.M. 1973. Mechanics of growth of some laccolithic intrusions in
555 the Henry Mountains, Utah, II: bending and failure of overburden layers and sill formation.
556 *Tectonophysics*, **18**, 311-354.
557

558 Reeve, M.T., Jackson, C.A.L., Bell, R.E., Magee, C. & Bastow, I.D. 2016. The stratigraphic
559 record of prebreakup geodynamics: Evidence from the Barrow Delta, offshore Northwest
560 Australia. *Tectonics*, **35**, 1935-1968.
561

562 Reeve, M.T., Magee, C., Bastow, I.D., McDermott, C., Jackson, C.A.-L., Bell, R.E. &
563 Prytulak, J. 2021. Nature of the Cuvier Abyssal Plain crust, offshore NW Australia. *Journal*
564 *of the Geological Society*, **178**, jgs2020-172.
565

566 Reeves, J., Magee, C. & Jackson, C.A.L. 2018. Unravelling intrusion-induced forced fold
567 kinematics and ground deformation using 3D seismic reflection data. *Volcanica*, **1**, 1-17.
568

569 Rey, S.S., Planke, S., Symonds, P.A. & Faleide, J.I. 2008. Seismic volcanostratigraphy of the
570 Gascoyne margin, Western Australia. *Journal of Volcanology and Geothermal Research*,
571 **172**, 112-131.
572

573 Rohrman, M. 2013. Intrusive large igneous provinces below sedimentary basins: An example
574 from the Exmouth Plateau (NW Australia). *Journal of Geophysical Research: Solid Earth*,
575 **118**, 4477-4487.
576

577 Rohrman, M. 2015. Delineating the Exmouth mantle plume (NW Australia) from denudation
578 and magmatic addition estimates. *Lithosphere*, L445. 441.
579

580 Schmiedel, T., Kjoberg, S., Planke, S., Magee, C., Galland, O., Schofield, N., Jackson, C.A.-
581 L. & Jerram, D.A. 2017. Mechanisms of overburden deformation associated with the
582 emplacement of the Tulipan sill, mid-Norwegian margin. *Interpretation*, **5**, SK23-SK38.
583

584 Segall, P. 2013. Volcano deformation and eruption forecasting. In: Pyle, D. M., Mather, T. A.
585 & Biggs, J. (eds) *Remote Sensing of Volcanoes and Volcanic Processes:
586 Integrating Observation and Modelling*. Geological Society, London, Special Publications,
587 **380**, 85-106.
588

589 Sigmundsson, F., Parks, M., Pedersen, R., Jónsdóttir, K., Ófeigsson, B.G., Grapenthin, R.,
590 Dumont, S., Einarsson, P., *et al.* 2018. Magma movements in volcanic plumbing systems and
591 their associated ground deformation and seismic patterns. In: Burchardt, S. (ed) *Volcanic and
592 igneous plumbing systems*. Elsevier, 285-322.
593

594 Skogly, O. 1998. *Seismic characterization and emplacement of intrusives in the Vøring
595 Basin*. M.Sc. Thesis, University of Oslo.
596

597 Smallwood, J.R. & Maresh, J. 2002. The properties, morphology and distribution of igneous
598 sills: modelling, borehole data and 3D seismic from the Faroe-Shetland area. In: Jolley, D.W.
599 & Bell, B.R. (eds) *The North Atlantic Igneous Province: Stratigraphy, tectonic, Volcanic and
600 Magmatic Processes*. Geological Society, London, Special Publications, **197**, 271-306.
601

602 Stagg, H., Alcock, M., Bernardel, G., Moore, A., Symonds, P. & Exon, N. 2004. *Geological
603 framework of the outer Exmouth Plateau and adjacent ocean basins*. Geoscience Australia,
604 169 p..
605

606 Steel, R., Olsen, T., Armentrout, J. & Rosen, N. 2002. Clinoforms, clinoform trajectories and
607 deepwater sands. *Sequence-stratigraphic models for exploration and production: Evolving
608 methodology, emerging models and application histories: Gulf Coast Section SEPM 22nd
609 Research Conference, Houston, Texas*, 367-381.
610

611 Symonds, P.A., Planke, S., Frey, O. & Skogseid, J. 1998. Volcanic evolution of the Western
612 Australian Continental Margin and its implications for basin development. *The Sedimentary
613 Basins of Western Australia 2: Proc. of Petroleum Society Australia Symposium, Perth, WA*,
614 33-53.
615

616 Thomson, K. & Schofield, N. 2008. Lithological and structural controls on the emplacement
617 and morphology of sills in sedimentary basins. In: Thomson, K. & Petford, N. (eds) *Structure
618 and Emplacement of High-Level Magmatic Systems*. Geological Society, London, Special
619 Publications, **302**, 31-44.
620

621 Tindale, K., Newell, N., Keall, J. & Smith, N. 1998. Structural evolution and charge history
622 of the Exmouth Sub-basin, northern Carnarvon Basin, Western Australia. *The Sedimentary*

623 *Basins of Western Australia 2: Proc. of Petroleum Society Australia Symposium, Perth, WA,*
624 *473-490.*
625
626 Trude, J., Cartwright, J., Davies, R.J. & Smallwood, J.R. 2003. New technique for dating
627 igneous sills. *Geology*, **31**, 4.
628
629 van Wyk de Vries, B., Márquez, A., Herrera, R., Bruña, J.G., Llanes, P. & Delcamp, A. 2014.
630 Craters of elevation revisited: forced-folds, bulging and uplift of volcanoes. *Bulletin of*
631 *Volcanology*, **76**, 1-20.
632
633 Widess, M. 1973. How thin is a thin bed? *Geophysics*, **38**, 1176-1180.
634
635 Willcox, J. & Exon, N.J. 1976. The regional geology of the Exmouth Plateau. *The APPEA*
636 *Journal*, **16**, 1-11.
637
638

Figure 1

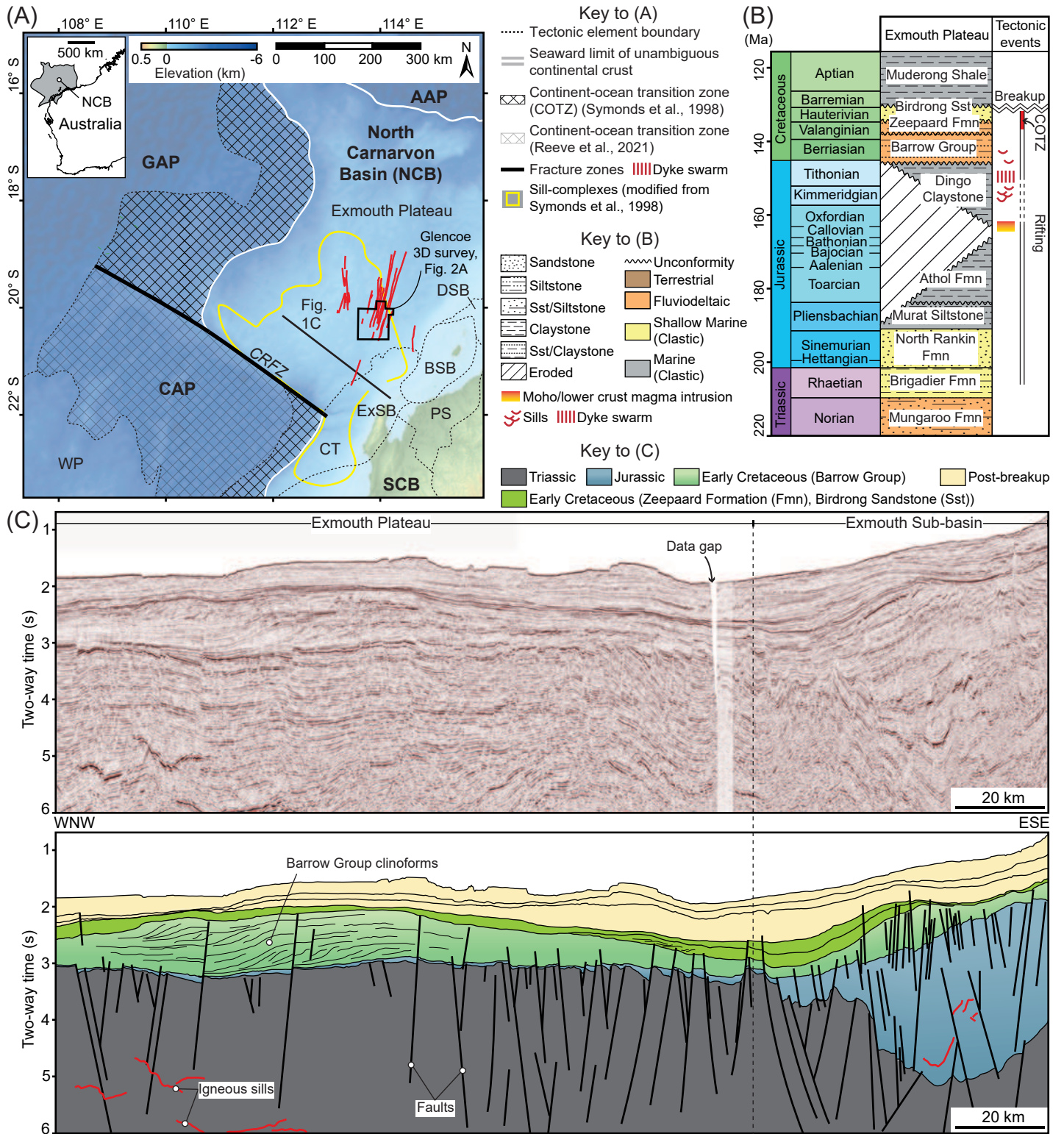


Figure 2

(A) Top Mungaroo Formation

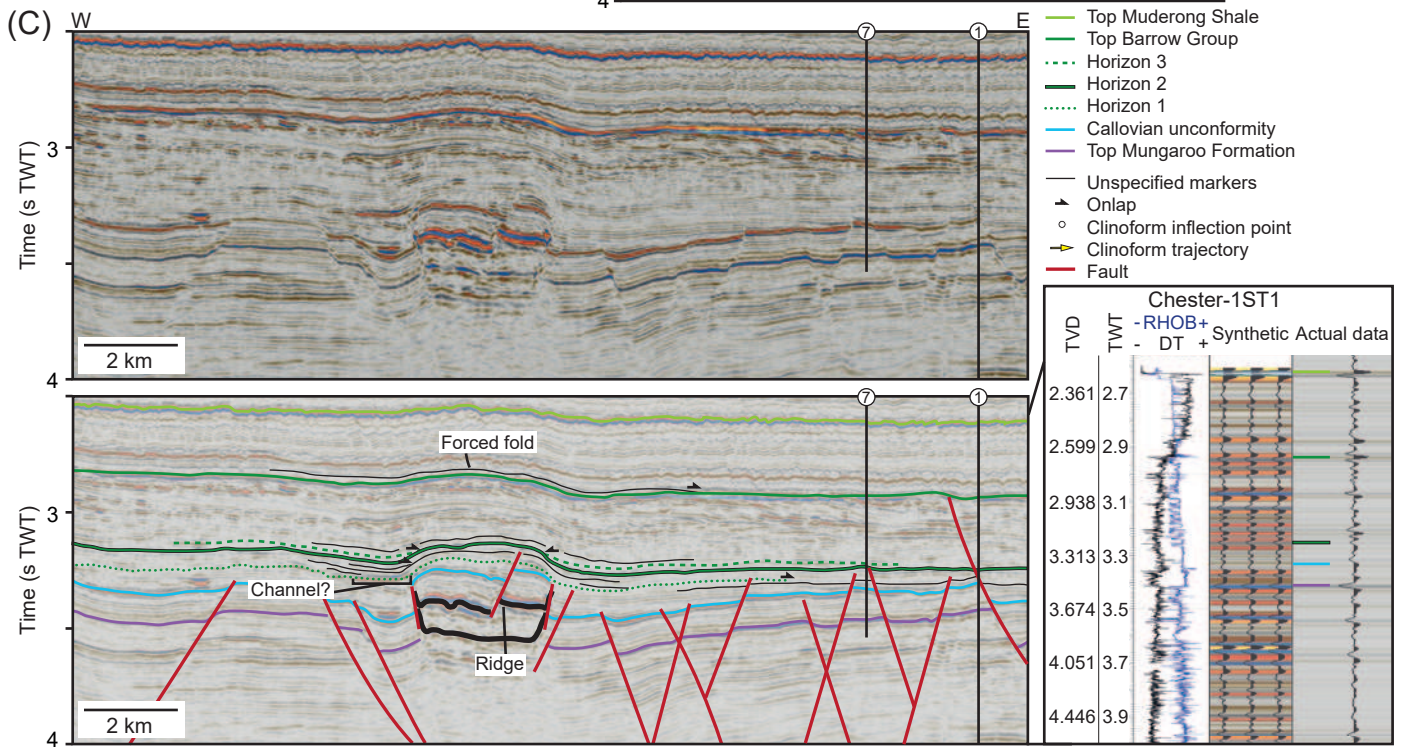
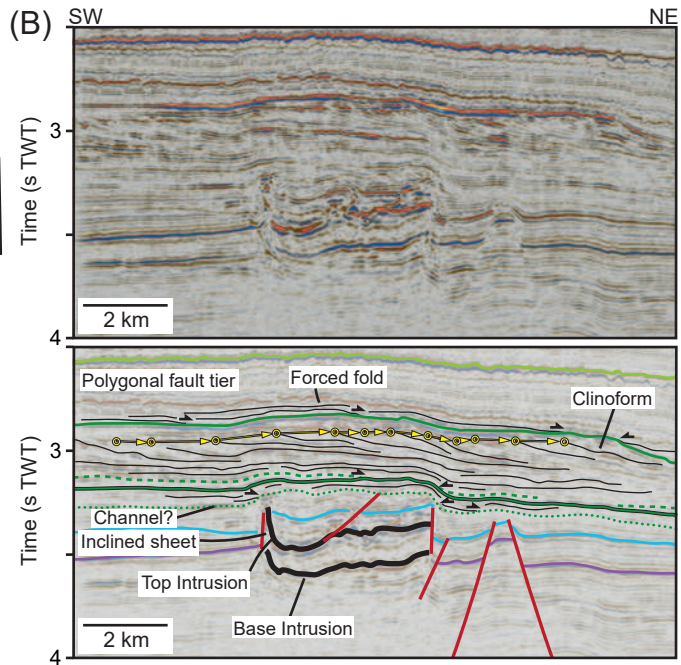
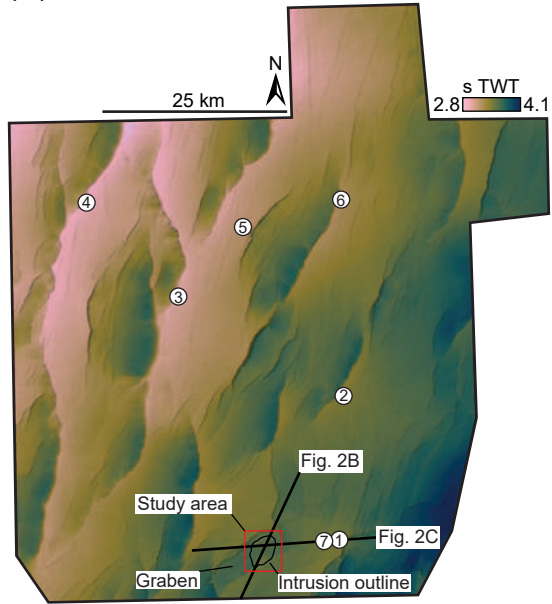


Figure 3

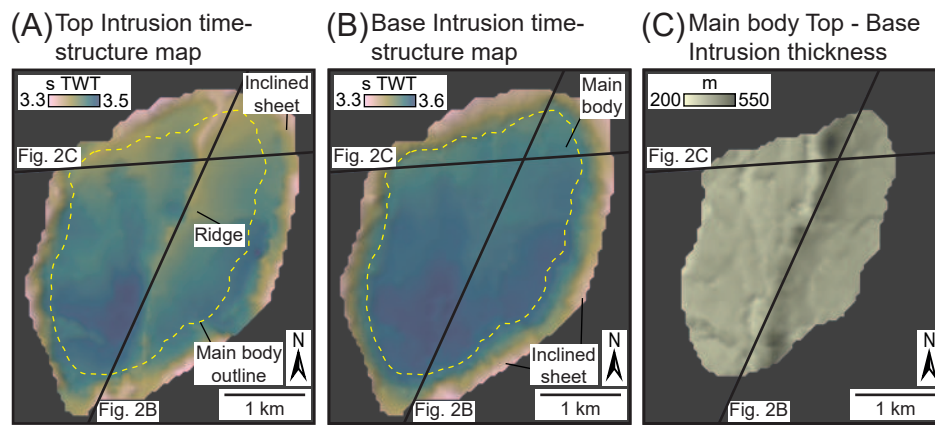


Figure 4

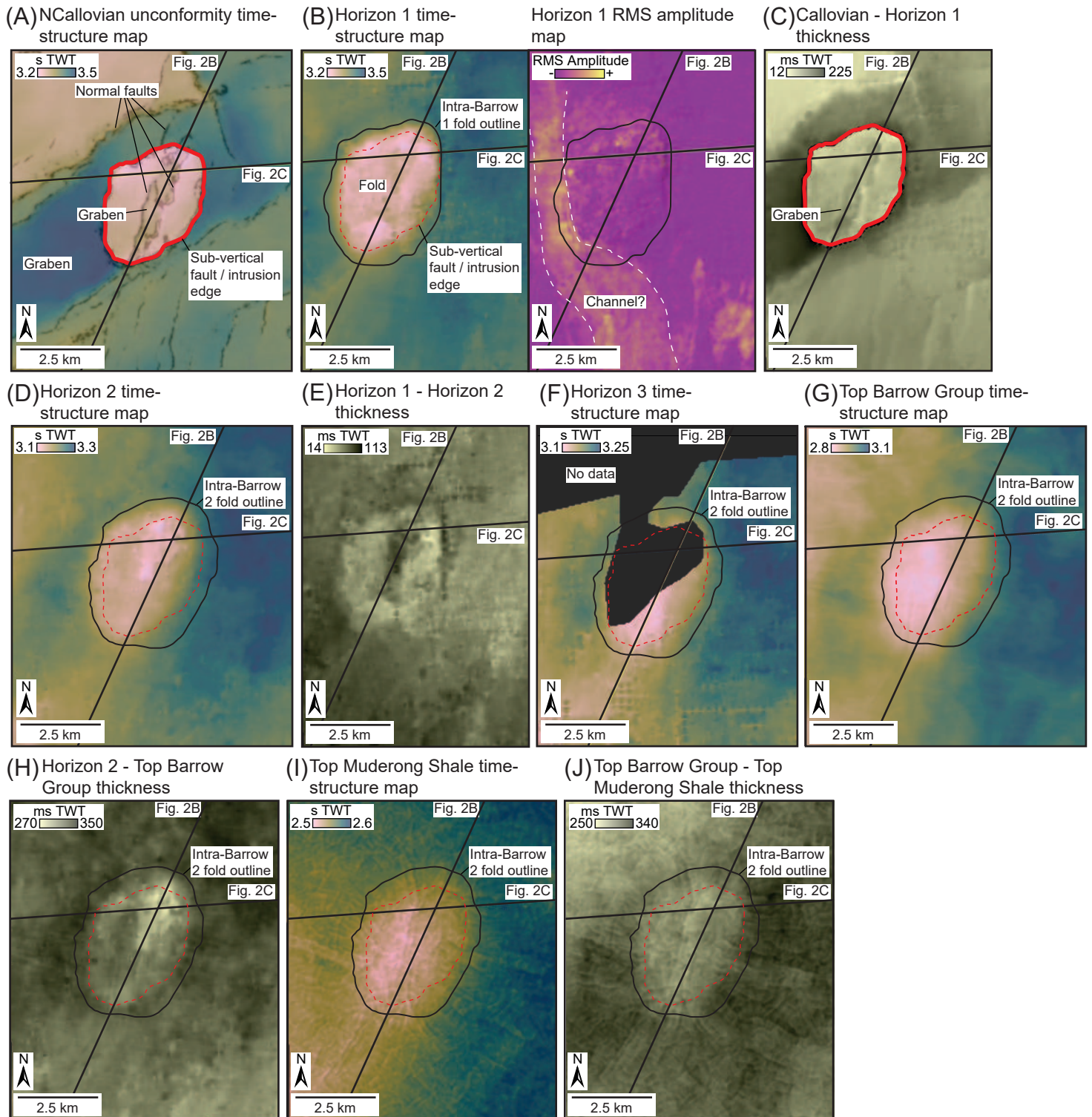
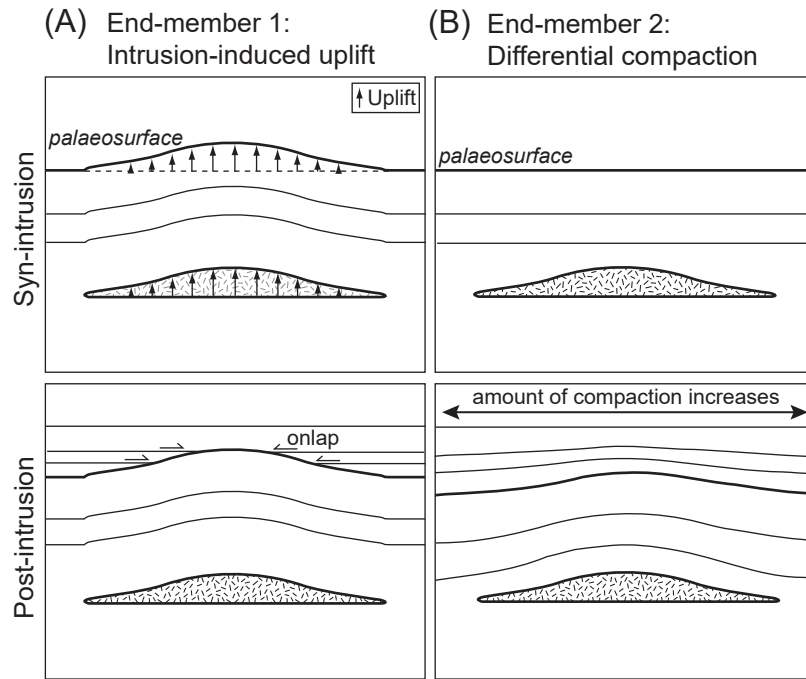


Figure 5



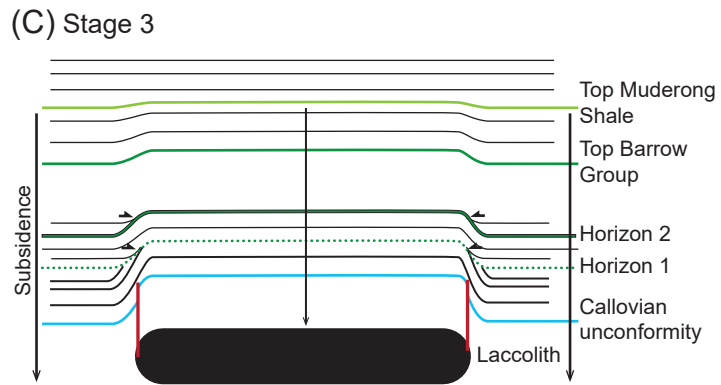
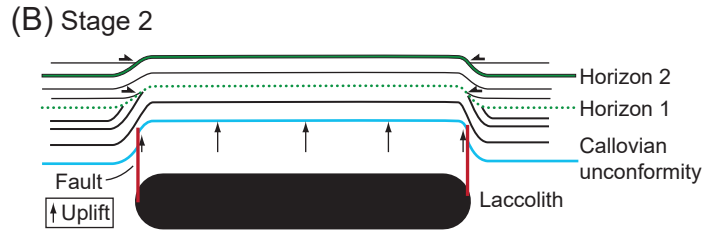
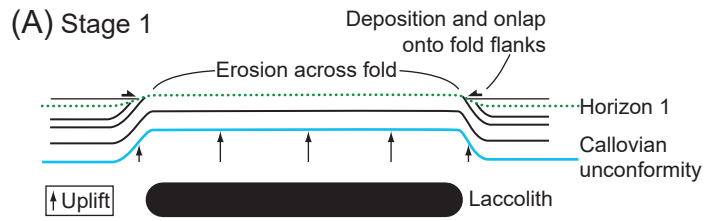
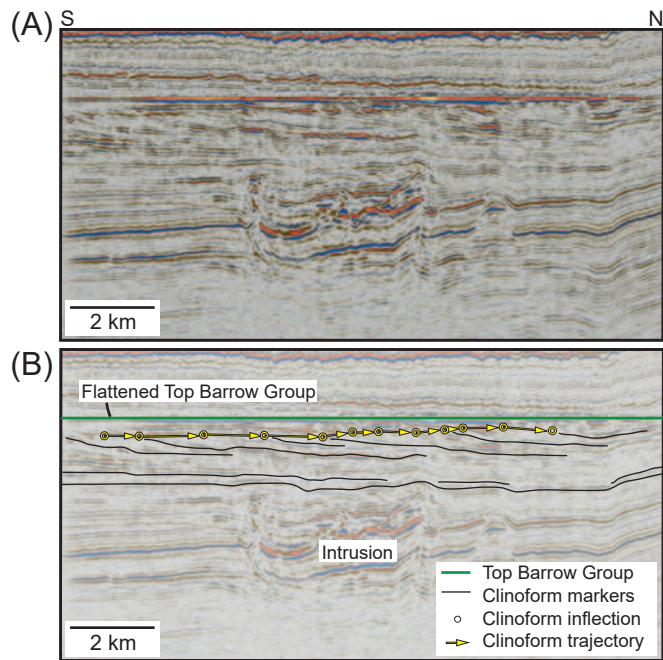
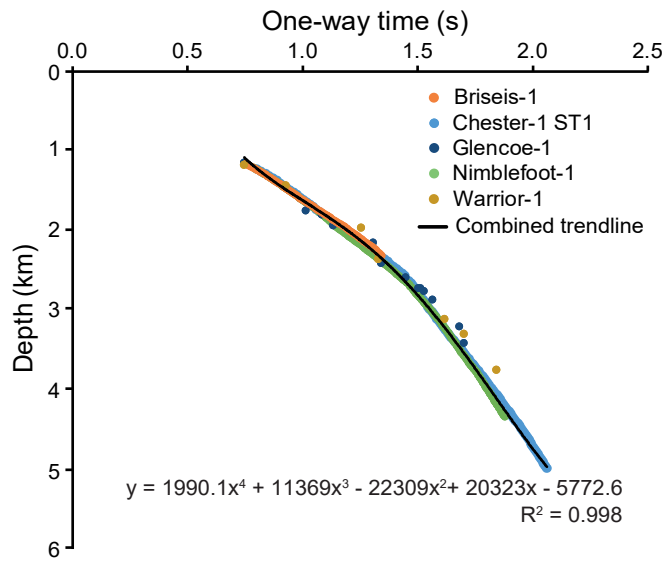


Figure 7





Supplementary Figure 1: Time-depth data for the five wells used in the study. Fitting a fourth-order polynomial trend-line through the cumulative data, and extrapolating it downwards, allows us to define seismic velocities at any depth.

Supplementary Table 1: Well checkshot data

Briseis-1			Chester-1 ST1			Glencoe-1			Nimblefoot-1			Two-way Time
Two-way Time	One-way Time	Measured depth	Two-way Time	One-way Time	Measured depth	Two-way Time	One-way Time	Measured depth	Two-way Time	One-way Time	Measured depth	[TWT]
[TWT]	[OWT]	[MD]	[TWT]	[OWT]	[MD]	[TWT]	[OWT]	[MD]	[TWT]	[OWT]	[MD]	[TWT]
(s)	(s)	(m)	(s)	(s)	(m)	(s)	(s)	(m)	(s)	(s)	(m)	(s)
1.520	0.760	1166.2	1.595	0.797	1225.0	1.500	0.750	1150.2	1.582	0.791	1214.5	1.500
1.540	0.770	1181.3	1.630	0.815	1255.0	2.035	1.018	1749.0	1.602	0.801	1229.1	1.860
1.558	0.779	1196.4	1.667	0.834	1285.0	2.172	1.086	1798.3	1.621	0.810	1244.3	2.510
1.579	0.789	1211.5	1.700	0.850	1315.0	2.272	1.136	1939.5	1.639	0.819	1259.4	2.660
1.597	0.799	1226.7	1.735	0.868	1345.0	2.616	1.308	2149.5	1.657	0.828	1274.5	3.230
1.615	0.808	1241.8	1.767	0.883	1375.0	2.684	1.342	2405.5	1.674	0.837	1289.2	3.400
1.634	0.817	1256.8	1.798	0.899	1405.0	2.900	1.450	2585.0	1.691	0.845	1304.3	3.680
1.651	0.825	1271.9	1.824	0.912	1435.0	3.004	1.502	2721.5	1.707	0.854	1319.4	
1.670	0.835	1287.1	1.851	0.925	1465.0	3.024	1.512	2721.5	1.723	0.861	1334.5	
1.687	0.844	1302.2	1.881	0.940	1495.0	3.056	1.528	2756.8	1.737	0.868	1349.2	
1.705	0.852	1317.0	1.913	0.957	1525.0	3.129	1.565	2868.5	1.753	0.876	1364.3	
1.721	0.861	1332.1	1.941	0.971	1555.0	3.363	1.682	3201.0	1.768	0.884	1379.4	
1.738	0.869	1347.3	1.972	0.986	1585.0	3.400	1.700	3410.0	1.784	0.892	1394.5	
1.753	0.877	1362.4	1.999	0.999	1615.0				1.800	0.900	1409.2	
1.768	0.884	1377.6	2.027	1.014	1645.0				1.817	0.908	1424.3	
1.783	0.892	1392.7	2.055	1.028	1675.0				1.832	0.916	1439.4	
1.799	0.900	1407.8	2.083	1.042	1705.0				1.847	0.923	1454.5	
1.815	0.907	1423.0	2.110	1.055	1735.0				1.861	0.931	1469.0	
1.832	0.916	1438.3	2.139	1.070	1765.0				1.877	0.938	1484.1	
1.848	0.924	1453.4	2.167	1.084	1795.0				1.891	0.946	1499.2	
1.863	0.932	1468.5	2.196	1.098	1825.0				1.905	0.953	1514.4	
1.878	0.939	1483.6	2.224	1.112	1855.0				1.919	0.960	1529.1	
1.892	0.946	1498.8	2.253	1.126	1885.0				1.935	0.967	1544.3	
1.906	0.953	1514.0	2.285	1.142	1915.0				1.949	0.975	1559.4	
1.920	0.960	1529.1	2.315	1.158	1945.0				1.964	0.982	1574.5	
1.934	0.967	1544.2	2.345	1.173	1975.0				1.978	0.989	1589.2	
1.949	0.975	1559.2	2.375	1.188	2005.0				1.993	0.997	1604.3	
1.964	0.982	1574.4	2.406	1.203	2035.0				2.009	1.004	1619.4	
1.980	0.990	1589.5	2.435	1.218	2065.0				2.024	1.012	1634.5	
1.995	0.998	1604.6	2.464	1.232	2095.0				2.039	1.019	1649.1	
2.012	1.006	1619.7	2.491	1.246	2125.0				2.053	1.027	1664.3	
2.028	1.014	1634.8	2.517	1.258	2155.0				2.069	1.034	1679.4	
2.044	1.022	1649.9	2.542	1.271	2185.0				2.083	1.042	1694.5	
2.059	1.030	1665.0	2.570	1.285	2215.0				2.099	1.049	1709.2	
2.076	1.038	1680.2	2.598	1.299	2245.0				2.114	1.057	1724.3	
2.093	1.047	1695.3	2.676	1.338	2335.0				2.127	1.064	1739.4	
2.108	1.054	1710.5	2.703	1.352	2365.0				2.140	1.070	1754.5	
2.123	1.062	1725.6	2.730	1.365	2395.0				2.152	1.076	1769.2	
2.138	1.069	1740.7	2.756	1.378	2425.0				2.165	1.082	1784.3	
2.155	1.077	1755.8	2.782	1.391	2455.0				2.177	1.089	1799.4	
2.171	1.086	1771.0	2.807	1.403	2485.0				2.189	1.095	1814.5	
2.187	1.094	1786.1	2.832	1.416	2515.0				2.202	1.101	1829.2	
2.204	1.102	1801.2	2.856	1.428	2545.0				2.214	1.107	1844.3	

2.222	1.111	1816.3
2.236	1.118	1831.5
2.252	1.126	1846.6
2.268	1.134	1861.6
2.283	1.142	1876.7
2.301	1.150	1891.8
2.316	1.158	1907.0
2.334	1.167	1922.1
2.351	1.176	1937.2
2.367	1.184	1952.3
2.382	1.191	1967.5
2.396	1.198	1982.5
2.409	1.205	1997.6
2.422	1.211	2012.8
2.437	1.219	2027.9
2.451	1.226	2043.1
2.466	1.233	2058.2
2.481	1.240	2073.4
2.495	1.247	2088.5
2.508	1.254	2103.6
2.524	1.262	2118.7
2.538	1.269	2133.9
2.551	1.276	2149.0
2.565	1.283	2164.2
2.580	1.290	2179.3
2.595	1.297	2194.4
2.609	1.305	2209.5
2.623	1.311	2224.6
2.635	1.317	2239.7
2.646	1.323	2254.8
2.657	1.329	2269.9
2.668	1.334	2285.0
2.680	1.340	2300.1
2.692	1.346	2315.2

2.878	1.439	2575.0
2.916	1.458	2635.0
2.934	1.467	2665.0
2.950	1.475	2695.0
2.964	1.482	2725.0
2.979	1.490	2755.0
2.994	1.497	2785.0
3.007	1.504	2815.0
3.022	1.511	2845.0
3.037	1.519	2875.0
3.052	1.526	2905.0
3.067	1.534	2935.0
3.083	1.542	2965.0
3.099	1.550	2995.0
3.115	1.557	3025.0
3.130	1.565	3055.0
3.146	1.573	3085.0
3.161	1.581	3115.0
3.177	1.589	3145.0
3.193	1.597	3175.0
3.209	1.604	3205.0
3.224	1.612	3235.0
3.240	1.620	3265.0
3.256	1.628	3295.0
3.272	1.636	3325.0
3.288	1.644	3355.0
3.306	1.653	3385.0
3.324	1.662	3415.0
3.342	1.671	3445.0
3.359	1.679	3475.0
3.375	1.687	3505.0
3.390	1.695	3535.0
3.405	1.702	3565.0
3.422	1.711	3595.0
3.439	1.719	3625.0
3.455	1.728	3655.0
3.471	1.736	3685.0
3.488	1.744	3715.0
3.505	1.753	3745.0
3.522	1.761	3775.0
3.539	1.769	3805.0
3.555	1.778	3835.0
3.571	1.786	3865.0
3.587	1.793	3895.0
3.602	1.801	3925.0
3.618	1.809	3955.0
3.634	1.817	3985.0
3.650	1.825	4015.0
3.666	1.833	4045.0

2.225	1.113	1859.4
2.237	1.118	1874.5
2.247	1.124	1889.2
2.259	1.130	1904.3
2.271	1.136	1919.4
2.284	1.142	1934.5
2.298	1.149	1949.1
2.295	1.147	1949.2
2.312	1.156	1964.3
2.309	1.154	1964.3
2.325	1.163	1979.4
2.322	1.161	1979.4
2.338	1.169	1994.5
2.334	1.167	1994.5
2.349	1.175	2009.1
2.363	1.181	2024.3
2.377	1.188	2039.4
2.390	1.195	2054.5
2.403	1.201	2069.2
2.417	1.209	2084.3
2.432	1.216	2099.4
2.446	1.223	2114.5
2.460	1.230	2129.1
2.474	1.237	2144.3
2.489	1.244	2159.4
2.503	1.251	2174.5
2.516	1.258	2189.1
2.530	1.265	2204.3
2.543	1.271	2219.4
2.556	1.278	2234.5
2.569	1.284	2249.1
2.582	1.291	2264.3
2.596	1.298	2279.4
2.609	1.305	2294.5
2.622	1.311	2309.1
2.635	1.317	2324.3
2.648	1.324	2339.4
2.661	1.330	2354.5
2.673	1.337	2369.2
2.686	1.343	2384.3
2.699	1.350	2399.4
2.712	1.356	2414.5
2.725	1.362	2429.2
2.738	1.369	2444.3
2.750	1.375	2459.4
2.763	1.381	2474.5
2.775	1.388	2489.1
2.788	1.394	2504.3
2.801	1.401	2519.4

3.682	1.841	4075.0
3.697	1.848	4105.0
3.711	1.856	4135.0
3.727	1.863	4165.0
3.742	1.871	4195.0
3.757	1.878	4225.0
3.772	1.886	4255.0
3.787	1.894	4285.0
3.803	1.901	4315.0
3.818	1.909	4345.0
3.833	1.917	4375.0
3.848	1.924	4405.0
3.864	1.932	4435.0
3.878	1.939	4465.0
3.893	1.946	4495.0
3.907	1.954	4525.0
3.921	1.961	4555.0
3.935	1.968	4585.0
3.949	1.975	4615.0
3.962	1.981	4645.0
3.976	1.988	4675.0
3.988	1.994	4705.0
4.002	2.001	4735.0
4.015	2.008	4765.0
4.029	2.014	4795.0
4.043	2.021	4825.0
4.056	2.028	4855.0
4.069	2.034	4885.0
4.080	2.040	4915.0
4.090	2.045	4945.0
4.103	2.051	4975.0
4.116	2.058	5005.0

2.814	1.407	2534.5
2.826	1.413	2549.2
2.838	1.419	2564.3
2.851	1.425	2579.4
2.863	1.431	2594.5
2.873	1.436	2609.1
2.875	1.438	2609.2
2.885	1.442	2624.2
2.887	1.443	2624.3
2.896	1.448	2639.4
2.898	1.449	2639.4
2.908	1.454	2654.5
2.910	1.455	2654.5
2.921	1.460	2669.1
2.930	1.465	2684.3
2.940	1.470	2699.4
2.950	1.475	2714.5
2.957	1.479	2729.1
2.965	1.482	2744.3
2.973	1.486	2759.4
2.981	1.490	2774.5
2.988	1.494	2789.1
2.998	1.499	2804.3
3.007	1.503	2819.4
3.017	1.509	2834.5
3.025	1.512	2849.2
3.034	1.517	2864.3
3.044	1.522	2879.4
3.053	1.527	2894.5
3.061	1.531	2909.2
3.071	1.535	2924.3
3.081	1.540	2939.4
3.088	1.544	2954.5
3.097	1.548	2969.1
3.107	1.553	2984.2
3.117	1.559	2999.3
3.125	1.562	3014.5
3.134	1.567	3029.1
3.142	1.571	3044.2
3.151	1.575	3059.4
3.159	1.580	3074.5
3.167	1.583	3089.1
3.176	1.588	3104.2
3.184	1.592	3119.3
3.192	1.596	3134.5
3.201	1.600	3149.1
3.209	1.604	3164.2
3.216	1.608	3179.3
3.223	1.612	3194.5

3.230	1.615	3209.1
3.239	1.619	3224.2
3.245	1.622	3239.3
3.252	1.626	3254.5
3.259	1.629	3269.1
3.266	1.633	3284.3
3.273	1.637	3299.4
3.280	1.640	3314.5
3.287	1.643	3329.1
3.294	1.647	3344.2
3.302	1.651	3359.4
3.308	1.654	3374.5
3.315	1.658	3389.1
3.324	1.662	3404.3
3.330	1.665	3419.4
3.337	1.669	3434.5
3.344	1.672	3449.1
3.351	1.676	3464.3
3.359	1.679	3479.4
3.365	1.683	3494.5
3.372	1.686	3509.1
3.378	1.689	3524.3
3.386	1.693	3539.4
3.394	1.697	3554.5
3.402	1.701	3569.2
3.410	1.705	3584.3
3.417	1.708	3599.4
3.425	1.712	3614.5
3.432	1.716	3629.1
3.440	1.720	3644.3
3.447	1.724	3659.4
3.454	1.727	3674.5
3.462	1.731	3689.1
3.470	1.735	3704.2
3.478	1.739	3719.3
3.487	1.744	3734.4
3.497	1.748	3749.1
3.504	1.752	3764.2
3.512	1.756	3779.4
3.519	1.759	3794.5
3.526	1.763	3809.1
3.533	1.767	3824.2
3.540	1.770	3839.3
3.546	1.773	3854.5
3.552	1.776	3869.1
3.559	1.779	3884.2
3.565	1.782	3899.3
3.571	1.786	3914.5
3.578	1.789	3929.1

3.584	1.792	3944.2
3.591	1.796	3959.4
3.598	1.799	3974.5
3.605	1.803	3989.1
3.612	1.806	4004.2
3.619	1.809	4019.4
3.625	1.812	4034.5
3.630	1.815	4049.1
3.638	1.819	4064.3
3.644	1.822	4079.4
3.650	1.825	4094.5
3.657	1.829	4109.1
3.664	1.832	4124.2
3.670	1.835	4139.3
3.676	1.838	4154.5
3.682	1.841	4169.1
3.689	1.845	4184.3
3.695	1.848	4199.4
3.702	1.851	4214.5
3.708	1.854	4229.1
3.716	1.858	4244.2
3.722	1.861	4259.4
3.729	1.865	4274.5
3.736	1.868	4289.2
3.743	1.871	4304.3
3.749	1.875	4319.4
3.756	1.878	4334.6

Vertical line 1

Vertical line 2

Vertical line 3

Vertical line 4

Vertical line 5

|

|

|

|

|

|

|

|

|

|

|

|

|

|

|

|

Warrior-1		All data		
One-way Time	Measured depth	Two-way Time	One-way Time	Measured depth
[OWT]	[MD]	[TWT]	[OWT]	[MD]
(s)	(m)	(s)	(s)	(m)
0.750	1172.1	1.520	0.760	1166.2
0.930	1429.2	1.540	0.770	1181.3
1.255	1959.6	1.558	0.779	1196.4
1.330	2356.5	1.579	0.789	1211.5
1.615	3106.0	1.597	0.799	1226.7
1.700	3293.2	1.615	0.808	1241.8
1.840	3748.0	1.634	0.817	1256.8
		1.651	0.825	1271.9
		1.670	0.835	1287.1
		1.687	0.844	1302.2
		1.705	0.852	1317.0
		1.721	0.861	1332.1
		1.738	0.869	1347.3
		1.753	0.877	1362.4
		1.768	0.884	1377.6
		1.783	0.892	1392.7
		1.799	0.900	1407.8
		1.815	0.907	1423.0
		1.832	0.916	1438.3
		1.848	0.924	1453.4
		1.863	0.932	1468.5
		1.878	0.939	1483.6
		1.892	0.946	1498.8
		1.906	0.953	1514.0
		1.920	0.960	1529.1
		1.934	0.967	1544.2
		1.949	0.975	1559.2
		1.964	0.982	1574.4
		1.980	0.990	1589.5
		1.995	0.998	1604.6
		2.012	1.006	1619.7
		2.028	1.014	1634.8
		2.044	1.022	1649.9
		2.059	1.030	1665.0
		2.076	1.038	1680.2
		2.093	1.047	1695.3
		2.108	1.054	1710.5
		2.123	1.062	1725.6
		2.138	1.069	1740.7
		2.155	1.077	1755.8
		2.171	1.086	1771.0
		2.187	1.094	1786.1
		2.204	1.102	1801.2

2.222	1.111	1816.3
2.236	1.118	1831.5
2.252	1.126	1846.6
2.268	1.134	1861.6
2.283	1.142	1876.7
2.301	1.150	1891.8
2.316	1.158	1907.0
2.334	1.167	1922.1
2.351	1.176	1937.2
2.367	1.184	1952.3
2.382	1.191	1967.5
2.396	1.198	1982.5
2.409	1.205	1997.6
2.422	1.211	2012.8
2.437	1.219	2027.9
2.451	1.226	2043.1
2.466	1.233	2058.2
2.481	1.240	2073.4
2.495	1.247	2088.5
2.508	1.254	2103.6
2.524	1.262	2118.7
2.538	1.269	2133.9
2.551	1.276	2149.0
2.565	1.283	2164.2
2.580	1.290	2179.3
2.595	1.297	2194.4
2.609	1.305	2209.5
2.623	1.311	2224.6
2.635	1.317	2239.7
2.646	1.323	2254.8
2.657	1.329	2269.9
2.668	1.334	2285.0
2.680	1.340	2300.1
2.692	1.346	2315.2
1.595	0.797	1225.0
1.630	0.815	1255.0
1.667	0.834	1285.0
1.700	0.850	1315.0
1.735	0.868	1345.0
1.767	0.883	1375.0
1.798	0.899	1405.0
1.824	0.912	1435.0
1.851	0.925	1465.0
1.881	0.940	1495.0
1.913	0.957	1525.0
1.941	0.971	1555.0
1.972	0.986	1585.0
1.999	0.999	1615.0
2.027	1.014	1645.0

2.055	1.028	1675.0
2.083	1.042	1705.0
2.110	1.055	1735.0
2.139	1.070	1765.0
2.167	1.084	1795.0
2.196	1.098	1825.0
2.224	1.112	1855.0
2.253	1.126	1885.0
2.285	1.142	1915.0
2.315	1.158	1945.0
2.345	1.173	1975.0
2.375	1.188	2005.0
2.406	1.203	2035.0
2.435	1.218	2065.0
2.464	1.232	2095.0
2.491	1.246	2125.0
2.517	1.258	2155.0
2.542	1.271	2185.0
2.570	1.285	2215.0
2.598	1.299	2245.0
2.676	1.338	2335.0
2.703	1.352	2365.0
2.730	1.365	2395.0
2.756	1.378	2425.0
2.782	1.391	2455.0
2.807	1.403	2485.0
2.832	1.416	2515.0
2.856	1.428	2545.0
2.878	1.439	2575.0
2.916	1.458	2635.0
2.934	1.467	2665.0
2.950	1.475	2695.0
2.964	1.482	2725.0
2.979	1.490	2755.0
2.994	1.497	2785.0
3.007	1.504	2815.0
3.022	1.511	2845.0
3.037	1.519	2875.0
3.052	1.526	2905.0
3.067	1.534	2935.0
3.083	1.542	2965.0
3.099	1.550	2995.0
3.115	1.557	3025.0
3.130	1.565	3055.0
3.146	1.573	3085.0
3.161	1.581	3115.0
3.177	1.589	3145.0
3.193	1.597	3175.0
3.209	1.604	3205.0

3.224	1.612	3235.0
3.240	1.620	3265.0
3.256	1.628	3295.0
3.272	1.636	3325.0
3.288	1.644	3355.0
3.306	1.653	3385.0
3.324	1.662	3415.0
3.342	1.671	3445.0
3.359	1.679	3475.0
3.375	1.687	3505.0
3.390	1.695	3535.0
3.405	1.702	3565.0
3.422	1.711	3595.0
3.439	1.719	3625.0
3.455	1.728	3655.0
3.471	1.736	3685.0
3.488	1.744	3715.0
3.505	1.753	3745.0
3.522	1.761	3775.0
3.539	1.769	3805.0
3.555	1.778	3835.0
3.571	1.786	3865.0
3.587	1.793	3895.0
3.602	1.801	3925.0
3.618	1.809	3955.0
3.634	1.817	3985.0
3.650	1.825	4015.0
3.666	1.833	4045.0
3.682	1.841	4075.0
3.697	1.848	4105.0
3.711	1.856	4135.0
3.727	1.863	4165.0
3.742	1.871	4195.0
3.757	1.878	4225.0
3.772	1.886	4255.0
3.787	1.894	4285.0
3.803	1.901	4315.0
3.818	1.909	4345.0
3.833	1.917	4375.0
3.848	1.924	4405.0
3.864	1.932	4435.0
3.878	1.939	4465.0
3.893	1.946	4495.0
3.907	1.954	4525.0
3.921	1.961	4555.0
3.935	1.968	4585.0
3.949	1.975	4615.0
3.962	1.981	4645.0
3.976	1.988	4675.0

3.988	1.994	4705.0
4.002	2.001	4735.0
4.015	2.008	4765.0
4.029	2.014	4795.0
4.043	2.021	4825.0
4.056	2.028	4855.0
4.069	2.034	4885.0
4.080	2.040	4915.0
4.090	2.045	4945.0
4.103	2.051	4975.0
4.116	2.058	5005.0
1.500	0.750	1150.2
2.035	1.018	1749.0
2.172	1.086	1798.3
2.272	1.136	1939.5
2.616	1.308	2149.5
2.684	1.342	2405.5
2.900	1.450	2585.0
3.004	1.502	2721.5
3.024	1.512	2721.5
3.056	1.528	2756.8
3.129	1.565	2868.5
3.363	1.682	3201.0
3.400	1.700	3410.0
1.582	0.791	1214.5
1.602	0.801	1229.1
1.621	0.810	1244.3
1.639	0.819	1259.4
1.657	0.828	1274.5
1.674	0.837	1289.2
1.691	0.845	1304.3
1.707	0.854	1319.4
1.723	0.861	1334.5
1.737	0.868	1349.2
1.753	0.876	1364.3
1.768	0.884	1379.4
1.784	0.892	1394.5
1.800	0.900	1409.2
1.817	0.908	1424.3
1.832	0.916	1439.4
1.847	0.923	1454.5
1.861	0.931	1469.0
1.877	0.938	1484.1
1.891	0.946	1499.2
1.905	0.953	1514.4
1.919	0.960	1529.1
1.935	0.967	1544.3
1.949	0.975	1559.4
1.964	0.982	1574.5

1.978	0.989	1589.2
1.993	0.997	1604.3
2.009	1.004	1619.4
2.024	1.012	1634.5
2.039	1.019	1649.1
2.053	1.027	1664.3
2.069	1.034	1679.4
2.083	1.042	1694.5
2.099	1.049	1709.2
2.114	1.057	1724.3
2.127	1.064	1739.4
2.140	1.070	1754.5
2.152	1.076	1769.2
2.165	1.082	1784.3
2.177	1.089	1799.4
2.189	1.095	1814.5
2.202	1.101	1829.2
2.214	1.107	1844.3
2.225	1.113	1859.4
2.237	1.118	1874.5
2.247	1.124	1889.2
2.259	1.130	1904.3
2.271	1.136	1919.4
2.284	1.142	1934.5
2.298	1.149	1949.1
2.295	1.147	1949.2
2.312	1.156	1964.3
2.309	1.154	1964.3
2.325	1.163	1979.4
2.322	1.161	1979.4
2.338	1.169	1994.5
2.334	1.167	1994.5
2.349	1.175	2009.1
2.363	1.181	2024.3
2.377	1.188	2039.4
2.390	1.195	2054.5
2.403	1.201	2069.2
2.417	1.209	2084.3
2.432	1.216	2099.4
2.446	1.223	2114.5
2.460	1.230	2129.1
2.474	1.237	2144.3
2.489	1.244	2159.4
2.503	1.251	2174.5
2.516	1.258	2189.1
2.530	1.265	2204.3
2.543	1.271	2219.4
2.556	1.278	2234.5
2.569	1.284	2249.1

2.582	1.291	2264.3
2.596	1.298	2279.4
2.609	1.305	2294.5
2.622	1.311	2309.1
2.635	1.317	2324.3
2.648	1.324	2339.4
2.661	1.330	2354.5
2.673	1.337	2369.2
2.686	1.343	2384.3
2.699	1.350	2399.4
2.712	1.356	2414.5
2.725	1.362	2429.2
2.738	1.369	2444.3
2.750	1.375	2459.4
2.763	1.381	2474.5
2.775	1.388	2489.1
2.788	1.394	2504.3
2.801	1.401	2519.4
2.814	1.407	2534.5
2.826	1.413	2549.2
2.838	1.419	2564.3
2.851	1.425	2579.4
2.863	1.431	2594.5
2.873	1.436	2609.1
2.875	1.438	2609.2
2.885	1.442	2624.2
2.887	1.443	2624.3
2.896	1.448	2639.4
2.898	1.449	2639.4
2.908	1.454	2654.5
2.910	1.455	2654.5
2.921	1.460	2669.1
2.930	1.465	2684.3
2.940	1.470	2699.4
2.950	1.475	2714.5
2.957	1.479	2729.1
2.965	1.482	2744.3
2.973	1.486	2759.4
2.981	1.490	2774.5
2.988	1.494	2789.1
2.998	1.499	2804.3
3.007	1.503	2819.4
3.017	1.509	2834.5
3.025	1.512	2849.2
3.034	1.517	2864.3
3.044	1.522	2879.4
3.053	1.527	2894.5
3.061	1.531	2909.2
3.071	1.535	2924.3

3.081	1.540	2939.4
3.088	1.544	2954.5
3.097	1.548	2969.1
3.107	1.553	2984.2
3.117	1.559	2999.3
3.125	1.562	3014.5
3.134	1.567	3029.1
3.142	1.571	3044.2
3.151	1.575	3059.4
3.159	1.580	3074.5
3.167	1.583	3089.1
3.176	1.588	3104.2
3.184	1.592	3119.3
3.192	1.596	3134.5
3.201	1.600	3149.1
3.209	1.604	3164.2
3.216	1.608	3179.3
3.223	1.612	3194.5
3.230	1.615	3209.1
3.239	1.619	3224.2
3.245	1.622	3239.3
3.252	1.626	3254.5
3.259	1.629	3269.1
3.266	1.633	3284.3
3.273	1.637	3299.4
3.280	1.640	3314.5
3.287	1.643	3329.1
3.294	1.647	3344.2
3.302	1.651	3359.4
3.308	1.654	3374.5
3.315	1.658	3389.1
3.324	1.662	3404.3
3.330	1.665	3419.4
3.337	1.669	3434.5
3.344	1.672	3449.1
3.351	1.676	3464.3
3.359	1.679	3479.4
3.365	1.683	3494.5
3.372	1.686	3509.1
3.378	1.689	3524.3
3.386	1.693	3539.4
3.394	1.697	3554.5
3.402	1.701	3569.2
3.410	1.705	3584.3
3.417	1.708	3599.4
3.425	1.712	3614.5
3.432	1.716	3629.1
3.440	1.720	3644.3
3.447	1.724	3659.4

3.454	1.727	3674.5
3.462	1.731	3689.1
3.470	1.735	3704.2
3.478	1.739	3719.3
3.487	1.744	3734.4
3.497	1.748	3749.1
3.504	1.752	3764.2
3.512	1.756	3779.4
3.519	1.759	3794.5
3.526	1.763	3809.1
3.533	1.767	3824.2
3.540	1.770	3839.3
3.546	1.773	3854.5
3.552	1.776	3869.1
3.559	1.779	3884.2
3.565	1.782	3899.3
3.571	1.786	3914.5
3.578	1.789	3929.1
3.584	1.792	3944.2
3.591	1.796	3959.4
3.598	1.799	3974.5
3.605	1.803	3989.1
3.612	1.806	4004.2
3.619	1.809	4019.4
3.625	1.812	4034.5
3.630	1.815	4049.1
3.638	1.819	4064.3
3.644	1.822	4079.4
3.650	1.825	4094.5
3.657	1.829	4109.1
3.664	1.832	4124.2
3.670	1.835	4139.3
3.676	1.838	4154.5
3.682	1.841	4169.1
3.689	1.845	4184.3
3.695	1.848	4199.4
3.702	1.851	4214.5
3.708	1.854	4229.1
3.716	1.858	4244.2
3.722	1.861	4259.4
3.729	1.865	4274.5
3.736	1.868	4289.2
3.743	1.871	4304.3
3.749	1.875	4319.4
3.756	1.878	4334.6
1.500	0.750	1172.1
1.860	0.930	1429.2
2.510	1.255	1959.6
2.660	1.330	2356.5

	3.230	1.615	3106.0
	3.400	1.700	3293.2
	3.680	1.840	3748.0